

Analytical relationships for the mechanical properties of additively manufactured porous biomaterials based on octahedral unit cells

Hedayati, Reza; Sadighi, M; Mohammadi-Aghdam, M; Zadpoor, Amir

DOI

[10.1016/j.apm.2017.01.076](https://doi.org/10.1016/j.apm.2017.01.076)

Publication date

2017

Document Version

Accepted author manuscript

Published in

Applied Mathematical Modelling: simulation and computation for engineering and environmental systems

Citation (APA)

Hedayati, R., Sadighi, M., Mohammadi-Aghdam, M., & Zadpoor, A. (2017). Analytical relationships for the mechanical properties of additively manufactured porous biomaterials based on octahedral unit cells. *Applied Mathematical Modelling: simulation and computation for engineering and environmental systems*, 46, 408-422. <https://doi.org/10.1016/j.apm.2017.01.076>

Important note

To cite this publication, please use the final published version (if applicable).
Please check the document version above.

Copyright

Other than for strictly personal use, it is not permitted to download, forward or distribute the text or part of it, without the consent of the author(s) and/or copyright holder(s), unless the work is under an open content license such as Creative Commons.

Takedown policy

Please contact us and provide details if you believe this document breaches copyrights.
We will remove access to the work immediately and investigate your claim.

Original article

Analytical relationships for the mechanical properties of additively manufactured porous biomaterials based on octahedral unit cells

R. Hedayati^{1,2*}, M. Sadighi¹, M. Mohammadi-Aghdam¹, A.A. Zadpoor²

¹*Department of Mechanical Engineering, Amirkabir University of Technology (Tehran Polytechnic), Hafez Ave, Tehran, Iran*

²*Department of Biomechanical Engineering, Faculty of Mechanical, Maritime, and Materials Engineering, Delft University of Technology (TU Delft), Mekelweg 2, 2628 CD, Delft, The Netherlands*

¹ Corresponding author, email: rezahedayati@gmail.com, r.hedayati@tudelft.nl, rezahedayati@aut.ac.ir, Tel: +31-15-2781021.

Abstract

Additively manufacturing (AM) techniques make it possible to fabricate open-cell interconnected structures with precisely controllable micro-architectures. It has been shown that the morphology, pore size, and relative density of a porous structure determine its macro-scale homogenized mechanical properties and, thus, its biological performance as a biomaterial. In this study, we used analytical, numerical, and experimental techniques to study the elastic modulus, Poisson's ratio, and yield stress of AM porous biomaterials made by repeating the same octahedral unit cell in all spatial directions. Analytical relationships were obtained based on both Euler-Bernoulli and Timoshenko beam theories by studying a single unit cell experiencing the loads and boundary conditions sensed in an infinite lattice structure. Both single unit cells and corresponding lattice structures were manufactured using AM and mechanically tested under compression to determine the experimental values of mechanical properties. Finite element models of both single unit cell and lattice structure were also built to estimate their mechanical properties numerically. Differences in the bulk mechanical properties of struts built in different directions were observed experimentally and were taken into account in derivation of the analytical solutions. Although the analytical and numerical results were generally in good agreement, the mechanical properties obtained by the Timoshenko beam theory were closer to numerical results. The maximum difference between analytical and numerical results for elastic modulus and Poisson's ratio was below 6%, while for yield stress it was about 13%, both occurring at the relative density of 50%. The maximum difference between the analytical and experimental values of the elastic modulus was <15% (relative density = 50%).

Keywords: Additive manufacturing, Porous biomaterials, Elastic properties, Octahedral, Finite element, Analytical solution

1. INTRODUCTION

Design of advanced biomaterials that replace tissues either permanently (e.g. implants) or temporarily (e.g. tissue engineering scaffolds) have been receiving expanding attention as of late. That is partially due to the availability of advanced manufacturing techniques such as additive manufacturing (3D printing) that make it possible to fabricate porous structures with complex micro-architectures [1-3]. The complex micro-structure of such biomaterials determines their large-scale properties including not only the mechanical properties [4] but also fluid transport properties such as permeability [5, 6] and biological properties such as the tissue regeneration performance [7-10]. Although the type of material/alloy from which these complex micro-architectures are made also play a role [11], the effects of geometrical features on the relevant properties of porous biomaterials remain paramount regardless of the material type.

It is therefore imperative to study the relationship between the micro-geometrical features of additively manufactured (AM) porous structures and their macroscopic properties. One of the most important types of such properties is the mechanical properties including both quasi-static [12] and fatigue resistance [13]. Previous studies of our group as well as other groups have shown that both above-mentioned types of mechanical properties severely depend on the geometrical features of the porous biomaterial [1, 4, 13-15], which are also referred to in the literature as the micro-architecture or topology [16] of such biomaterials. The type and dimensions of the unit cell, which when repeated in different directions, creates the porous structure are found to be particularly important [17].

Space-filling polyhedra and their derivatives are among the most important types of the basic unit cells used for design of AM porous biomaterials. Ideally, designers would like to have access to simple analytical relationships or computational models that could be used to estimate

the mechanical properties of porous structures based on all important types of (space-filling) polyhedra. The availability of such relationships or computational models allows for rational design of such biomaterials, where the choice of unit cell type and dimensions (e.g. pore size and porosity) is based on accurate predictions of the resulting mechanical properties. That is why there has been a surge of concern in topology-property relationships of porous structures made from different unit cell types. For example, the mechanical response of porous structures made with the cube [18], rhombic dodecahedron [19-21], tetrakaidecahedrons [22, 23], diamond [24], body-centered cubic structure (BCC) [25], pyramidal [26], rhombicuboctahedron [27], truncated cube [28], and truncated cuboctahedron [29] unit cells have been studied analytically, numerically, and experimentally [30-32].

The current study advances the above-mentioned line of research by addressing the topology-property relationship for a new unit cell, namely the octahedral unit cell, to expand the library of unit cells from which the basic unit cells can be chosen. An extensive library of unit cells to choose from is particularly important for the design of biomaterials where not only the mechanical properties but also other types of biologically relevant properties need to be simultaneously taken into account.

The octahedral unit cell (Figure 1) is a morphology that has not been studied thoroughly in the past. Two earlier studies [33, 34] have studied a simpler version of this unit cell where the horizontal struts (struts BB' , $B'B''$, $B''B'''$, and $B'''B$ in Figure 1) which are important in the structure strength are excluded. Presence of the horizontal struts also has the advantage of making the lattice structure isotropic. Moreover, the agreement between analytical, numerical, and experimental results were not optimal in both the above-mentioned studies.

In this study, analytical, numerical, and experimental approaches are used to study the elastic mechanical properties (elastic modulus, Poisson's ratio, and yield stress) of AM porous biomaterials based on octahedral unit cell. Analytical relationships (based on both Euler-Bernoulli and Timoshenko beam theories) are obtained for one unit cell with boundary and loading conditions identical to that of a unit cell located inside a lattice structure. As for the analytical study, we used a methodology similar to the ones used in our previous works on other unit cell types [27-29]. Finite element models were also built for both single unit cells and lattice structures based on the octahedral unit cell. Similar specimens were fabricated using AM and mechanically tested to obtain experimental results. The results of the analytical, numerical, and experimental approaches were compared to each other to investigate the accuracy of the presented analytical relationships and numerical models.

2 MATERIALS AND METHODS

2.1 Analytical formulas

2.1.1 Relative density

Relative density is defined as the proportion of the porous structure density to the bulk material density. The relative density can be obtained by calculating the volume occupied by the material inside a porous structure and dividing it by the total volume of the porous structure. Each octahedral unit cell possesses 12 struts each having length l and cross-sectional area A (Figure 1). Therefore, the total strut volume inside each unit cell is $12lA$. Since the dimensions of an octahedral unit cell are $l\sqrt{2}$, the total volume of the unit cell is $2\sqrt{2}l^3$. As a result, the relative density of the structure is calculated as

$$\mu = \frac{12lA}{2\sqrt{2}l^3} = 3\sqrt{2}\frac{A}{l^2} \quad (1)$$

This formula, however, does not consider the material overlay in the vertices (see the effects of mass multiple counting on the numerical results of different unit cell types in [35]). The actual relative density is lower than the value calculated in Eq. (1). Each unit cell with struts having circular cross-section is composed of 24 pieces shown in Figure 2. The volume of each of the pieces is equal to $0.5 \pi r^2 l - 3.707 r^3$. Therefore, the exact relative density of the octahedral unit cell is

$$\mu = \frac{24(0.5 \pi r^2 l - 2.575769 r^3)}{2\sqrt{2}l^3} = \frac{12 \pi r^2 l}{2\sqrt{2}l^3} - \frac{61.81846}{2\sqrt{2}l^3} = 3\sqrt{2}\pi \left(\frac{r}{l}\right)^2 - 21.85612 \left(\frac{r}{l}\right)^3 \quad (2)$$

2.1.2 Euler-Bernoulli theory

In order to obtain the elastic modulus, Poisson's ratio, and yield stress of an octahedral unit cell (which are identical to those of the octahedral lattice structure), the displacements of the unit cell vertices after applying an external load F must be determined first. To calculate the displacement of the vertices, the stiffness matrix of the unit cell is needed. The unit cell has a symmetric plane coinciding the square $BB'B''B'''$ (Figure 1). Moreover, due to the symmetry of the unit cell (and as a result its deformation) with respect to planes ABB'' and $AB'B'''$, point A can only move in the two noted planes, and as a result their intersection line. Consequently, point A can only move vertically (in the direction q_1 shown in Figure 1). Point B is located in both the symmetry planes ABB'' and $BB'B''B'''$. Therefore, point B (and its corresponding points B' , B'' , and B''') has only one degree of freedom (DOF) in the direction demonstrated in Figure 1 as q_2 . Therefore, the entire system has two DOFs. The first DOF consists of vertices A and A' , while the second DOF consists of vertices B, B' , B'' , and B''' . For plotting the free-body diagram of the system, only strut AB is considered. The deformations of the seven other inclined struts are similar to that of strut AB and their effects will be considered when calculating the elements of the stiffness matrix.

The angles of the ends of the struts remain unchanged during the unit cell deformation. That is because the vertices of the structure are rigid bodies. If the angles between the connected struts at a vertex are changed, it means that a plastic hinge is formed at the vertex whose investigation is beyond the scope of the current study. Since the angles of both ends of each strut in the unit cell remain constant during the simple compression of the unit cell, the general deformation of each strut can be considered as the summation of two distinct deformations at the free end of a cantilever beam. The forces and moments required to be applied at the free end of a cantilever beam to cause such pure extension and pure lateral displacement (without any additional rotation) is shown in Figure 3. This figure will be referred to several times in the next subsections.

Since the unit cell has two DOFs, the stiffness matrix of the system must be a 2×2 matrix. The elements of the stiffness matrix are obtained as follows. The first DOF is displaced ($q_1 = 1$) and the second DOF is kept fixed ($q_2 = 0$). The forces required to be applied to DOFs q_1 and q_2 to cause such a deformation determine the elements k_{11} and k_{21} of the stiffness matrix. Similarly, the forces required at each of the two DOFs to cause $q_2 = 1$ and $q_1 = 0$ determine the elements k_{12} and k_{22} of the stiffness matrix. It is assumed that the mechanical properties of the bulk material could be different for the horizontal and inclined struts [36]. The elements of the stiffness matrix are obtained in the remainder of this sub-section.

First DOF ($q_1 = 1$): In this deformation, points B, B', B'', and B''' are fixed, while points A and A' are displaced towards the symmetry plane by unity (Figure 4). This deformation for strut AB can be assumed to be the summation of two distinct deformations: a) contraction of strut AB by $\frac{\sqrt{2}}{2}$, and b) lateral displacement (without rotation) of its end A by $\frac{\sqrt{2}}{2}$ (Figure 4). The loads

required to cause such a deformation can be obtained from Figure 3 and are depicted in Figure 4.

Equilibrium of forces at point A in the y direction gives

$$\sum f_{y,A} = 0 \Rightarrow \frac{E_s A \sqrt{2} \sqrt{2}}{l} \frac{1}{2} \frac{1}{2} 4 + \frac{12 E_s I \sqrt{2} \sqrt{2}}{l^3} \frac{1}{2} \frac{1}{2} 4 - \frac{1}{2} Q_1 = 0 \Rightarrow Q_1 = k_{11} = \frac{4 A E_s}{l} + \frac{48 E_s I}{l^3} \quad (3)$$

In Eq. (3), $\frac{E_s A \sqrt{2} \sqrt{2}}{l} \frac{1}{2} \frac{1}{2}$ and $\frac{12 E_s I \sqrt{2} \sqrt{2}}{l^3} \frac{1}{2} \frac{1}{2}$ are multiplied by 4, because there are four similar struts connected to point A (see Figure 1). Similarly, in Eq. (3), Q_1 has been multiplied by $\frac{1}{2}$, because the force calculated at point A is $\frac{1}{2}$ of the total forces applied at the first DOF (because point A has a corresponding point at the lowermost part of the unit cell, denoted A'). On the other hand, equilibrium of forces in the x direction at point B gives

$$\sum f_{x,B} = 0 \Rightarrow \frac{E_s A \sqrt{2} \sqrt{2}}{l} \frac{1}{2} \frac{1}{2} 2 - \frac{12 E_s I \sqrt{2} \sqrt{2}}{l^3} \frac{1}{2} \frac{1}{2} 2 + \frac{1}{4} Q_2 = 0 \Rightarrow Q_2 = k_{21} = -\frac{4 A E_s}{l} + \frac{48 E_s I}{l^3} \quad (4)$$

In Eq. (4), $\frac{E_s A \sqrt{2} \sqrt{2}}{l} \frac{1}{2} \frac{1}{2}$ and $\frac{12 E_s I \sqrt{2} \sqrt{2}}{l^3} \frac{1}{2} \frac{1}{2}$ are multiplied by 2, because there are two similar inclined struts connected to point B (see Figure 1). Similarly, Q_2 is multiplied by $\frac{1}{4}$, because the force calculated at point B is $\frac{1}{4}$ of the total forces applied to the second DOF (because point B has three other corresponding points in the unit cell, denoted B', B'', and B''').

Second DOF ($q_2 = 1$): In this deformation, point A is fixed, while point B is displaced horizontally in the x direction (Figure 5). This deformation can be assumed to be the summation of two distinct deformations: a) expansion of strut AB by $\frac{\sqrt{2}}{2}$, and b) lateral displacement (without rotation) of its end B by $\frac{\sqrt{2}}{2}$ (Figure 5a). The equilibrium of forces at point A in the y direction yields

$$\sum f_{y,A} = 0 \Rightarrow -\frac{E_s A \sqrt{2} \sqrt{2}}{l} \frac{1}{2} \frac{1}{2} 4 + \frac{12 E_s I \sqrt{2} \sqrt{2}}{l^3} \frac{1}{2} \frac{1}{2} 4 - \frac{1}{2} Q_1 = 0 \Rightarrow Q_1 = k_{12} = -\frac{4 A E_s}{l} + \frac{48 E_s I}{l^3} \quad (5)$$

Due to this deformation, struts BB' and BB'' are also expanded by $\sqrt{2}$ (Figure 5b). Therefore, the equilibrium of forces in the x direction at point B yields

$$\begin{aligned} \sum f_{x,B} = 0 \quad \Rightarrow \quad & -\frac{E_s A \sqrt{2} \sqrt{2}}{l} \frac{2}{2} - \frac{12E_s I \sqrt{2} \sqrt{2}}{l^3} \frac{2}{2} - \frac{2A\gamma E_s \sqrt{2}}{l} \frac{\sqrt{2}}{2} + \frac{1}{4} Q_2 = 0 \quad \Rightarrow \quad Q_2 = k_{22} \\ & = \frac{4AE_s}{l} (1 + 2\gamma) + \frac{48E_s I}{l^3} \end{aligned} \quad (6)$$

where γ is the ratio of the bulk material elastic modulus in the horizontal direction (i.e. in struts BB' , $B'B''$, $B''B'''$, and $B'''B$) to that in the inclined struts. For a structure with equal mechanical properties in all the struts, $\gamma = 1$.

2.1.3 Timoshenko theory

Timoshenko beam theory takes shear deformation and rotational inertia effects into account, making it suitable for describing the behavior of short beams. The procedure of calculating the elements of the stiffness matrix using Timoshenko beam theory is very similar to that previously presented for Euler-Bernoulli beam theory. The only difference is that in the relationships presented in subsection 2.1.2, the lateral forces $\frac{12E_s I}{l^3}$ must be replaced by $\left(\frac{l^3}{12E_s I} + \frac{l}{2\kappa A G_s}\right)^{-1}$. The proof is stated in the following. The governing equations of a uniform beam (with constant cross-section) based on Timoshenko beam theory are:

$$\frac{d^2}{dx^2} \left(E_s I \frac{d\varphi}{dx} \right) = q(x, t) \quad (7)$$

$$\frac{dw}{dx} = \varphi - \frac{1}{\kappa A G_s} \frac{d}{dx} \left(E_s I \frac{d\varphi}{dx} \right)$$

where w is the lateral (in z-direction) deflection of the mid-surface, φ is the rotational angle of the normal to the mid-surface, and κ is the shear coefficient factor. The bending moment M_{xx} and shear force Q are in relation with the angle of rotation φ and displacement w by

$$M_{xx} = -E_s I \frac{\partial \varphi}{\partial x} \quad (8)$$

$$Q = \kappa A G_s \left(-\varphi + \frac{\partial w}{\partial x} \right)$$

If the only load applied to the cantilever Timoshenko beam is force P at its free end, Eqs. (7)

gives

$$\delta = \frac{Fl^3}{3E_s I} + \frac{Fl}{\kappa A G_s} \quad \text{and} \quad \theta = \frac{Fl^2}{2E_s I} + \frac{F}{\kappa A G_s} \quad (9)$$

In a cantilever beam at the free end of which a moment M is imposed, the displacement and rotation are identical to those of the corresponding Euler-Bernoulli beam. Due to the same reason as in the Euler-Bernoulli beam theory (the angle at the free end of the cantilever beam shown in Figure 3 must remain unchanged), the rotations produced by the load F and moment M at the free end of the beam must be equal and opposite. Therefore, the relationship between M and F is

$$\frac{Fl^2}{2E_s I} + \frac{F}{\kappa A G_s} = \frac{Ml}{E_s I} \quad \Rightarrow \quad M = F \left(\frac{l}{2} + \frac{E_s I}{\kappa A G_s l} \right) \quad (10)$$

The force F and moment M respectively tend to increase and decrease the lateral deflection. Consequently, the resulted lateral deflection caused by force F and moment M at the free end of the beam is given by

$$\delta = \frac{Fl^3}{3E_s I} + \frac{Fl}{\kappa A G_s} - \left(\frac{Fl}{2} + \frac{FE_s I}{\kappa A G_s l} \right) \frac{l^2}{2E_s I} = \frac{Fl^3}{12E_s I} + \frac{Fl}{2\kappa A G_s} \quad (11)$$

Rewriting (11) as a function of F gives

$$F = \frac{1}{\frac{l^3}{12E_s I} + \frac{l}{2\kappa A G_s}} \delta \quad (12)$$

Therefore for the Timoshenko beam theory, the lateral forces $\frac{12E_s I}{l^3} \delta$ in Figure 3a must be

replaced by $\left(\frac{l^3}{12E_s I} + \frac{l}{2\kappa A G_s} \right)^{-1} \delta$.

2.1.4 The obtained stiffness matrices

The load applied on the first DOF equals twice the external load applied to the unit cell, or $Q_1 = 2F$. Since the unit cells are free to move laterally, the external load on the second DOF is zero. Using the force and stiffness matrix elements obtained above, the force-displacement relationships for the Euler-Bernoulli and Timoshenko beam theories are respectively given by

$$\begin{Bmatrix} Q_1 \\ Q_2 \end{Bmatrix} = \begin{Bmatrix} 2F \\ 0 \end{Bmatrix} = \begin{bmatrix} \frac{4AE_s}{l} + \frac{48E_s I}{l^3} & -\frac{4AE_s}{l} + \frac{48E_s I}{l^3} \\ -\frac{4E_s A}{l} + \frac{48E_s I}{l^3} & \frac{4AE_s}{l}(1+2\gamma) + \frac{48E_s I}{l^3} \end{bmatrix} \begin{Bmatrix} q_1 \\ q_2 \end{Bmatrix} \quad (13)$$

and

$$\begin{Bmatrix} Q_1 \\ Q_2 \end{Bmatrix} = \begin{Bmatrix} 2F \\ 0 \end{Bmatrix} = \begin{bmatrix} \frac{4AE_s}{l} + \frac{4}{\frac{12E_s I}{l} + \frac{2\kappa AG_s}{l}} & -\frac{4AE_s}{l} + \frac{4}{\frac{12E_s I}{l} + \frac{2\kappa AG_s}{l}} \\ -\frac{4AE_s}{l} + \frac{4}{\frac{12E_s I}{l} + \frac{2\kappa AG_s}{l}} & \frac{4(1+2\gamma)AE_s}{l} + \frac{4}{\frac{12E_s I}{l} + \frac{2\kappa AG_s}{l}} \end{bmatrix} \begin{Bmatrix} q_1 \\ q_2 \end{Bmatrix} \quad (14)$$

Note that both these stiffness matrices are symmetric.

2.1.5 The elastic properties

The elastic modulus of a unit cell can be obtained by $E = \frac{P_u l_u}{A_u \delta_u}$ where l_u , A_u , and δ_u are the length, cross-sectional area, and axial displacement of the unit cell under an external axial load P_u . By replacing the corresponding values, we have

$$E = \frac{F}{(2q_1)l\sqrt{2}} \quad (15)$$

Inserting q_1 from the inverse of Eq. (13) into Eq. (15) and dividing it by the elastic modulus of the bulk material E_s yields the relative elastic modulus of the octahedral structure based on the Euler-Bernoulli beam theory as

$$\frac{E}{E_s} = \frac{\sqrt{2}A(24I + \gamma Al^2 + 12\gamma l)}{l^2(12I + Al^2 + 2A\gamma l^2)} \quad (16)$$

and for the Timoshenko beam theory as

$$\frac{E}{E_s} = \frac{\sqrt{2}A(12I\gamma + A\gamma\kappa l^2 + 24\kappa l + 12\gamma\kappa l + 12\gamma l\nu_s)}{l^2(A\kappa l^2 + 2\gamma A\kappa l^2 + 12I + 24\gamma l + 12I\kappa + 12l\nu_s + 24\gamma l\nu_s)} \quad (17)$$

Poisson's ratio is simply defined as the ratio of lateral and axial strains, which for our problem is equal to $\frac{q_2}{q_1}$. Substituting the corresponding values from the inverse of Eq. (13) into $\frac{q_2}{q_1}$ gives the

Poisson's ratio relationship for the Euler-Bernoulli beam theory as

$$v = \frac{Al^2 - 12I}{12I + Al^2 + 2\gamma Al^2} \quad (18)$$

and for the Timoshenko beam theory as

$$v = \frac{A\kappa l^2 + 12I - 12I\kappa + 12I\nu_s}{A\kappa l^2 + 2\gamma A\kappa l^2 + 12I + 24\gamma I + 12I\kappa + 12I\nu_s + 24\gamma I\nu_s} \quad (19)$$

For having the yield stress of the structure, first the maximum stress of the structure must be obtained. In a general displacement, the increase in the length of strut AB is

$$\delta_{axial} = (q_2 - q_1) \frac{\sqrt{2}}{2} \quad (20)$$

and the difference between the lateral displacements of its two ends A and B are

$$\delta_{lateral} = (q_2 + q_1) \frac{\sqrt{2}}{2} \quad (21)$$

Based on Eq. (20), the normal stress generated in the strut due to increase in its length is

$$\sigma_{axial} = \frac{E_s}{l} (q_2 - q_1) \frac{\sqrt{2}}{2} \quad (22)$$

On the other hand, the bending moment generated in the ends A and B of strut AB due to the differences in the lateral deflections of both ends of the strut is (see Figure 3)

$$M = \frac{6E_s I}{l^2} (q_2 + q_1) \frac{\sqrt{2}}{2} \quad (23)$$

and the resulted bending stress is $\frac{Mc}{I}$ which after inserting Eq. (23) gives

$$\sigma_{bending} = \frac{6E_s c}{l^2} (q_2 + q_1) \frac{\sqrt{2}}{2} \quad (24)$$

The maximum stress in the struts of the structure is therefore found by $\sigma_{axial} \pm \sigma_{bending}$. It was observed that $\sigma_{axial} - \sigma_{bending}$ has a larger magnitude than $\sigma_{axial} + \sigma_{bending}$ (which was

expected due to the fact that strut AB is most probably under compression when the unit cell is compressed, i.e. $\sigma_{axial} < 0$). The yield stress of the structure is obtained from a simple cross multiply: if an external stress $\sigma_{ext} = \frac{F}{(l\sqrt{2})^2}$ on the unit cell causes the maximum local stress in the struts reach $\sigma_{max} = \sigma_{axial} - \sigma_{bending}$, then the external yield stress which causes the local stress of the material reach the yield stress of bulk material σ_{ys} is $\sigma_y = \sigma_{ext} \sigma_{ys} / \sigma_{max}$ or $\sigma_y = \frac{F \sigma_{ys}}{(l\sqrt{2})^2 (\sigma_{axial} - \sigma_{bending})}$. After inserting q_1 and q_2 from the inverse of Eq. (13) into Eqs. (22)

and (24) and the resulting σ_{max} into $\frac{F \sigma_{ys}}{(l\sqrt{2})^2 \sigma_{max}}$, we have

$$\frac{\sigma_y}{\sigma_{ys}} = \frac{\sqrt{2}A}{l} \left[\frac{24I + \gamma Al^2 + 12\gamma I}{12Il + \gamma Al^3 + 6cAl^2(1 + \gamma)} \right] \quad (25)$$

for the Euler-Bernoulli beam theory and

$$\frac{\sigma_y}{\sigma_{ys}} = -\frac{\sqrt{2}A}{l} \left[\frac{(12\gamma I + 24 * I\kappa + 12\gamma I\kappa + 12\gamma I\nu_s + \gamma A\kappa l^2)}{(12\gamma Il(1 + \nu_s) + 12I\kappa + \gamma A\kappa l^3) + 6c(12I + \gamma Al^2)(1 + \gamma)(1 + \nu_s)} \right] \quad (26)$$

for the Timoshenko beam theory.

2.2. Finite element modeling

Two types of FE models were constructed: single unit cell structure and lattice structure. The load and boundary conditions in the FE single cell was set similar to that in the analytical approach. In the single unit cell model, the rotational movement of all the vertices were fixed in all the directions. Points B and B`` were free to move only in the X direction, and points B` and B```` were only free to move in the Z direction (Figure 1). Points A and A` were only allowed to move in the Y direction (Figure 1). A nodal downward vertical force was imposed on point A. In the lattice structure (Figure 6), the lowermost nodes of the structure were constraint vertically (i.e. in the Y direction) and all the uppermost nodes were moved downward in such a way that the lattice structure underwent 0.2 % strain. All of the top and bottom nodes were free to move in

the horizontal plane (i.e. in directions X and Z). One of the lowermost nodes of the lattice structure was constraint in all directions to prevent dynamic rigid body motions that could compromise the convergence of the solution.

The struts of both types of FE models were discretized using BEAM 189 element type in ANSYS which is based on the standard Timoshenko beam theory. Linear elastic material model with material properties similar to those of the bulk material used for manufacturing the test specimens were assigned to the elements. ANSYS nonlinear static solver was used to solve the FE models. To obtain the elastic modulus of the structures, the well-known formula $E =$

$\frac{P l_{structure}}{A_{structure} \delta_{structure}}$ was used, where $\delta_{structure}$ is the applied displacement on the lattice structure

(or the single unit cell), $l_{structure}$ and $A_{structure}$ are the length and cross-sectional area of the lattice structure (or the single unit cell), and P is the measured resultant force in the structure. For obtaining the Poisson's ratio, the lateral displacement was divided by the applied axial displacement. In order to obtain the relative yield stress, the maximum stress in the structure was

measured and then inserted in $\frac{P \sigma_{ys}}{l_{structure}^2 \sigma_{max}}$ (for proof, see the two sentences before Eq. (25)).

2.3. Experimental tests

5th generation Replicator Desktop Makerbot 3D printer with poly-lactic acid (PLA) filaments (khaki color) were used for manufacturing the test specimens. In order to have the mechanical properties of the filament bulk material, some cylindrical specimens were manufactured and tested before carrying out the experimental tests on octahedral unit cells. The cylinders were made in the horizontal and vertical directions as well as in a 45° angle with respect to the 3D printer platform (Figure 7, Table 1). Three specimens were manufactured for each cylinder type (totally nine specimens) all having the nominal lengths of 25.4 mm and diameters of 12.7 mm.

The extruder travel speed was set to 150 mm/s and the infill density was set to 100%. The layer thickness was set to 200 μm .

For the experimental tests on the octahedral structure, two sets of specimens: lattice (Figure 8) and single (Figure 9) octahedral structures were manufactured with different relative densities. For the single unit cells, five different strut radius to length ratios of 0.05, 0.1, 0.15, 0.2, 0.25 were chosen, and for each strut radius to length ratio, three specimens were made. For the lattice structure, four different strut radius to length ratios of 0.05, 0.1, 0.15, and 0.2 were considered. However, the manufactured specimens with $r/l=0.15$ had many defects and their results were omitted. The dimensions of all the single unit cell and lattice structure specimens were $4\times 4\times 4$ cm. The static compression tests were performed using an Instron ElectroPuls E10000 machine with a 10 kN load cells. The displacement rate was set to 0.2 mm/min.

3. RESULTS

The load-displacement curves of each set of test specimens were generally close to each other (Figure 10). The elastic moduli and yield stresses obtained from single and lattice test specimens were used for validation of the analytical and numerical results (Figure 11). The results of the single unit cell and lattice FE models were less than 1% different. Therefore, only the results pertaining to the FE lattice structure is reported here. The build orientation significantly influenced the obtained mechanical properties of the bulk material (Table 1) with as much as 25% difference between the smallest and largest values of the elastic modulus. Since the struts of the octahedral structure (Figure 1 and Figure 6) are mostly inclined, the bulk mechanical properties obtained from the 45° cylinder model was used for normalizing the experimental data. The data points presented in Figure 11 for the analytical solution are reported for uniform mechanical properties (i.e. $\gamma = 1$).

Comparison of the elastic properties (Figure 11) shows that all the analytical and numerical results are in good agreement, especially for relative densities below 0.4. Generally, the elastic properties obtained for the Timoshenko and Euler-Bernoulli beam theories were close. As the relative density of the structure increased, the difference between the analytical results obtained using the Euler-Bernoulli and Timoshenko beam theories increased. However, their maximum difference (at $\mu = 0.5$) did not exceed 6% for elastic modulus and Poisson's ratio and 10% for yield stress. Compared to the analytical results obtained using the Euler-Bernoulli theory, the mechanical properties estimated using the analytical solutions based on the Timoshenko beam theory were closer to the numerical results, which are also based on the Timoshenko beam theory.

As opposed to the elastic modulus and Poisson's ratio, the difference between the numerical and analytical values of yield stress values had an increasing, decreasing, and then again increasing trend (Figure 11c). The two values coincide at relative density around 26% (Figure 11c). The maximum difference between the numerical and analytical results was about 12% which occurred at $\mu = 0.6$. Another important observation is that at a relative density as large as 50%, the elastic modulus and yield stress of the octahedral structure do not exceed 14% of those of the bulk material.

The experimentally determined values of the elastic modulus of the "lattice" structures (Figure 11a) are generally close to the corresponding analytical solution based on the Timoshenko beam theory. For the relative density of 0.491, the experimental mean elastic modulus was 17% lower than the analytical solution. The agreement between experimental results and analytical solutions was improved for the experiments based on "single" unit cells. The experimental and analytical elastic modulus values almost coincided at the relative density of 0.033. They, however, start to

deviate from each other as the relative density increased (Figure 11a). The mean experimental elastic modulus of the single unit cell specimen was always larger than the analytical counterpart (Figure 11a). The maximum difference between the analytical and single unit cell experimental elastic moduli was about 9% which occurred at the relative density of 49.1%.

The experimental/analytical correlation was also good for the yield stress (Figure 11c). The obtained yield stresses from the lattice specimens were always below the Timoshenko beam theory analytical curve. Similar to the elastic modulus curves (Figure 11a), the yield stress obtained from the single unit cell specimens were mostly larger than those determined analytically with the only exception being for the relative density of 0.033. The maximum difference between the analytical solution and the experimental values of the yield stress for single unit cells was 16.5% which occurred at a relative density of 36%.

4. DISCUSSIONS

The advantage of analytical relationships is fast estimation of mechanical properties. That can be helpful in reducing the designing cost (the cost of evaluating the mechanical properties associated with different designs of porous structures in an optimal design scheme), effort, and time. The analytical relationships obtained here, which are the main contribution of this study, showed good agreement with numerical and experimental results. The parametric study of different effective parameters in a porous structure is much easier to be performed using analytical relationships, by which a designer can find the optimum relative density and pore size according to the required mechanical properties in an application. Moreover, the future numerical models based on octahedral micro-structure can be validated/benchmarked by comparing their results with the presented analytical relationships.

Although there was generally a good analytical/numerical/experimental correlation in this study, the experimental results deviated from analytical and numerical predictions at smaller relative densities (Figure 11a,c). As the strut diameters become smaller and comparable to the resolution of the AM process, the roughness of the surface plays more important role in deviation from theory [37]. Fine-tuning the analytical model to also include the roughness effects can lead to a great improvement in theory/experiment correlation. Related to this is the usage of advanced mechanical models for treating the behavior of joints in the lattice structure [38, 39]. Both process variation effects and joint behavior are important in explaining the discrepancies between model predictions and experimentally measured values.

Increasing the relative density increases the r/l ratio of struts. In thick beams, the effects of the shear and rotation inertia become important. Those effects are considered in the Timoshenko beam theory but are ignored in the Euler-Bernoulli beam theory. That is why the results of the Euler-Bernoulli and Timoshenko beams almost coincide at small relative densities but start to deviate as the relative density increases (Figure 11).

While the experimental results (i.e. the elastic modulus and yield stress) of the tested lattice structures were usually lower than both the analytical and numerical solutions, the experimental results of the single unit cells were usually slightly higher than the numerical and analytical values. The difference between the results of single unit cell specimens and the analytical solutions increased as the relative density increased. One of the main reasons for this increased elastic modulus is that as the relative density increases, more parts of the neighbor struts start to be aggregated at the vertices. Therefore, the free length of the struts (the portions of struts not touching parts of other struts) decreases. Since the corresponding material of the neighbor struts supports the material located at the ends of the vertices, they do not participate significantly in

the structure deformation. The resulted decrease in the deformation of the lattice structure decreases the deformation of the unit cell that leads to an increase in the elastic modulus of the lattice structure. The aggregation of the ends of the struts in the vertices was not taken into account in the analytical and numerical solutions in this study, and therefore they predicted lower stiffness values as compared to the experimental data. One way to take the effects of the aggregation of the ends of the struts into account is to replace the “vertex to vertex” length, l , in the analytical calculations with a reduced length $l_{reduced}$, where $l_{reduced}$ is the free length of the struts.

The elastic modulus of the bulk material is affected by the manufacturing direction of the material (Table 1). The elastic modulus of the bulk material in a direction parallel to the extruded filaments is 3.21% higher than that of the bulk material built with a 45° angle with respect to the extruded filaments. It was observed that by setting $\gamma = 1.0321$ in the analytical elastic properties relationships, the change in the elastic properties is small and therefore for this type of structure it cannot be the cause of deviation of the experimental and analytical solutions with respect to each other. The parameter γ can become important in structures for which the mechanical properties of the bulk material are substantially different in different directions. For example, if the build direction of the octahedral unit cells was parallel to the YZ direction rather than the XZ direction (Figure 1), the structure would have included vertically-built struts as well as struts built in the 45° direction. Since the mechanical properties of the vertically built struts is about 20% lower than that of the struts made in with a 45° angle, including the parameter γ in the analytical relationships could substantially change the estimated mechanical properties of the lattice structure.

The elastic modulus of an octahedral structure made of Ti-6Al-4V (which is one of the most well-known materials for biomedical applications, $E_s = 113.8 \text{ GPa}$) with 50% porosity is lower than 8 GPa (see Figure 11). This elastic modulus is around the stiffness values measured for human bone, see e.g. [40]. Therefore, porous biomaterials with octahedral unit cell type can successfully be used for large bone defects without causing stress shielding.

In this study, the mechanical properties of porous biomaterials based on the octahedral unit cell were obtained in the elastic range. One of the main application of these analytical relationships is in designing bone replacing scaffolds. Depending on the application, the porous biomaterials are also susceptible to other loading types such as transient, cycling, and impact loads. Obtaining analytical solutions for non-static loads in complex structures (such as porous biomaterials) are usually very laborious. In addition, the strain values may be different from those obtained analytically for the unit cells situated close to the boundaries of the lattice structure even for simple unit cells under simple loading scenarios. Experimental and numerical approaches are more effective in studying the above-mentioned cases of complex loading or non-uniform strain distribution. Recent advances in full-field strain measurement techniques such as Digital Image Correlation (DIC) which is an optical method for observing the full-field deformation of structure [41-45]) and finite element damage modeling (such as cohesive zone models which can efficiently model the crack propagation in different structures [46-48]) allow for better description of the deformation and failure in these structures under complex loads, and therefore better designs of the micro-architecture of porous biomaterials. In addition to mechanical aspects, permeability [5] and biological performance of porous biomaterials are also of great importance. In particular the type of unit cell determine the amount of the surface area of porous biomaterials. Since the surface of porous biomaterials could be used for improvement of their

bone regeneration performance [49], it is important to simultaneously consider all the relevant aspects including permeability, surface area, and mechanical properties when choosing the type of unit cell and the relative density of the porous biomaterial.

5. CONCLUSIONS

It was observed that the analytical results based on the Timoshenko beam theory are closer to the numerical results as compared to the analytical results based on the Euler-Bernoulli beam theory. There was generally good agreement between numerical and analytical results. The maximum difference between analytical and numerical results for elastic modulus and Poisson's ratio, which occurred at very large relative densities, was lower than 6%. The experimental results obtained from both single unit cells and lattice structures were also close to the derived analytical solutions. Introduction of porosity into the bulk material in the form of octahedral morphology led to a huge decrease in mechanical properties: for a relative density as large as 50%, the elastic modulus and yield stress of the octahedral structure did not exceed 14% of those of the bulk material.

REFERENCES

1. Heintl, P., L. Müller, C. Körner, R.F. Singer, and F.A. Müller, *Cellular Ti-6Al-4V structures with interconnected macro porosity for bone implants fabricated by selective electron beam melting*. Acta biomaterialia, 2008. **4**(5): p. 1536-1544.
2. Murr, L.E., S.M. Gaytan, E. Martinez, F. Medina, and R.B. Wicker, *Next generation orthopaedic implants by additive manufacturing using electron beam melting*. International journal of biomaterials, 2012. **2012**.
3. Vaezi, M., H. Seitz, and S. Yang, *A review on 3D micro-additive manufacturing technologies*. The International Journal of Advanced Manufacturing Technology, 2013. **67**(5-8): p. 1721-1754.
4. Zadpoor, A.A. and R. Hedayati, *Analytical relationships for prediction of the mechanical properties of additively manufactured porous biomaterials*. Journal of Biomedical Materials Research Part A, 2016.
5. Van Bael, S., Y.C. Chai, S. Truscello, M. Moesen, G. Kerckhofs, H. Van Oosterwyck, J.-P. Kruth, and J. Schrooten, *The effect of pore geometry on the in vitro biological behavior of human periosteum-derived cells seeded on selective laser-melted Ti6Al4V bone scaffolds*. Acta biomaterialia, 2012. **8**(7): p. 2824-2834.

6. Truscello, S., G. Kerckhofs, S. Van Bael, G. Pyka, J. Schrooten, and H. Van Oosterwyck, *Prediction of permeability of regular scaffolds for skeletal tissue engineering: a combined computational and experimental study*. Acta biomaterialia, 2012. **8**(4): p. 1648-1658.
7. Rumpler, M., A. Woesz, J.W. Dunlop, J.T. van Dongen, and P. Fratzl, *The effect of geometry on three-dimensional tissue growth*. Journal of the Royal Society Interface, 2008. **5**(27): p. 1173-1180.
8. Bidan, C.M., K.P. Kommareddy, M. Rumpler, P. Kollmannsberger, Y.J. Bréchet, P. Fratzl, and J.W. Dunlop, *How linear tension converts to curvature: geometric control of bone tissue growth*. PloS one, 2012. **7**(5): p. e36336.
9. Bidan, C.M., K.P. Kommareddy, M. Rumpler, P. Kollmannsberger, P. Fratzl, and J.W. Dunlop, *Geometry as a factor for tissue growth: towards shape optimization of tissue engineering scaffolds*. Advanced healthcare materials, 2013. **2**(1): p. 186-194.
10. Bidan, C.M., F.M. Wang, and J.W. Dunlop, *A three-dimensional model for tissue deposition on complex surfaces*. Computer methods in biomechanics and biomedical engineering, 2013. **16**(10): p. 1056-1070.
11. Wauthle, R., S.M. Ahmadi, S.A. Yavari, M. Mulier, A.A. Zadpoor, H. Weinans, J. Van Humbeeck, J.-P. Kruth, and J. Schrooten, *Revival of pure titanium for dynamically loaded porous implants using additive manufacturing*. Materials Science and Engineering: C, 2015. **54**: p. 94-100.
12. Sobral, J.M., S.G. Caridade, R.A. Sousa, J.F. Mano, and R.L. Reis, *Three-dimensional plotted scaffolds with controlled pore size gradients: effect of scaffold geometry on mechanical performance and cell seeding efficiency*. Acta Biomaterialia, 2011. **7**(3): p. 1009-1018.
13. Yavari, S.A., S. Ahmadi, R. Wauthle, B. Pouran, J. Schrooten, H. Weinans, and A. Zadpoor, *Relationship between unit cell type and porosity and the fatigue behavior of selective laser melted meta-biomaterials*. Journal of the mechanical behavior of biomedical materials, 2015. **43**: p. 91-100.
14. Li, S., Q. Xu, Z. Wang, W. Hou, Y. Hao, R. Yang, and L. Murr, *Influence of cell shape on mechanical properties of Ti-6Al-4V meshes fabricated by electron beam melting method*. Acta biomaterialia, 2014. **10**(10): p. 4537-4547.
15. Murr, L., K. Amato, S. Li, Y. Tian, X. Cheng, S. Gaytan, E. Martinez, P. Shindo, F. Medina, and R. Wicker, *Microstructure and mechanical properties of open-cellular biomaterials prototypes for total knee replacement implants fabricated by electron beam melting*. Journal of the mechanical behavior of biomedical materials, 2011. **4**(7): p. 1396-1411.
16. Wang, X., S. Xu, S. Zhou, W. Xu, M. Leary, P. Choong, M. Qian, M. Brandt, and Y.M. Xie, *Topological design and additive manufacturing of porous metals for bone scaffolds and orthopaedic implants: A review*. Biomaterials, 2016. **83**: p. 127-141.
17. Hollister, S.J., *Porous scaffold design for tissue engineering*. Nature materials, 2005. **4**(7): p. 518-524.
18. !!! INVALID CITATION !!! [3-5].
19. Shulmeister, V., M. Van der Burg, E. Van der Giessen, and R. Marissen, *A numerical study of large deformations of low-density elastomeric open-cell foams*. Mechanics of materials, 1998. **30**(2): p. 125-140.
20. Babaei, S., B.H. Jahromi, A. Ajdari, H. Nayeb-Hashemi, and A. Vaziri, *Mechanical properties of open-cell rhombic dodecahedron cellular structures*. Acta Materialia, 2012. **60**(6): p. 2873-2885.
21. Borleffs, M., *Finite element modeling to predict bulk mechanical properties of 3D printed metal foams*. 2012, TU Delft, Delft University of Technology.
22. Zheng, X., H. Lee, T.H. Weisgraber, M. Shusteff, J. DeOtte, E.B. Duoss, J.D. Kuntz, M.M. Biener, Q. Ge, and J.A. Jackson, *Ultralight, ultrastiff mechanical metamaterials*. Science, 2014. **344**(6190): p. 1373-1377.
23. Warren, W. and A. Kraynik, *Linear elastic behavior of a low-density Kelvin foam with open cells*. Journal of Applied Mechanics, 1997. **64**(4): p. 787-794.

24. Ahmadi, S., G. Campoli, S. Amin Yavari, B. Sajadi, R. Wauthlé, J. Schrooten, H. Weinans, and A.A. Zadpoor, *Mechanical behavior of regular open-cell porous biomaterials made of diamond lattice unit cells*. Journal of the mechanical behavior of biomedical materials, 2014. **34**: p. 106-115.
25. Smith, M., Z. Guan, and W. Cantwell, *Finite element modelling of the compressive response of lattice structures manufactured using the selective laser melting technique*. International Journal of Mechanical Sciences, 2013. **67**: p. 28-41.
26. Ptochos, E. and G. Labeas, *Elastic modulus and Poisson's ratio determination of micro-lattice cellular structures by analytical, numerical and homogenisation methods*. Journal of Sandwich Structures and Materials, 2012: p. 1099636212444285.
27. Hedayati, R., M. Sadighi, M. Mohammadi-Aghdam, and A.A. Zadpoor, *Mechanics of additively manufactured porous biomaterials based on the rhombicuboctahedron unit cell*. Journal of the Mechanical Behavior of Biomedical Materials, 2016. **53**: p. 272–294.
28. Hedayati, R., M. Sadighi, M. Mohammadi-Aghdam, and A.A. Zadpoor, *Mechanical properties of regular porous biomaterials made from truncated cube repeating unit cells: analytical solutions and computational models*. Materials Science and Engineering: C, 2016. **60**: p. 163-183.
29. Hedayati, R., M. Sadighi, M. Mohammadi-Aghdam, and A. Zadpoor, *Mechanical behavior of additively manufactured porous biomaterials made from truncated cuboctahedron unit cells*. International Journal of Mechanical Sciences, 2016. **106**: p. 19-38.
30. Doyoyo, M. and J.W. Hu, *Multi-axial failure of metallic strut-lattice materials composed of short and slender struts*. International journal of solids and structures, 2006. **43**(20): p. 6115-6139.
31. Wang, A.-J. and D. McDowell, *Yield surfaces of various periodic metal honeycombs at intermediate relative density*. International Journal of Plasticity, 2005. **21**(2): p. 285-320.
32. Deshpande, V.S., N.A. Fleck, and M.F. Ashby, *Effective properties of the octet-truss lattice material*. Journal of the Mechanics and Physics of Solids, 2001. **49**(8): p. 1747-1769.
33. Sun, J., Y. Yang, and D. Wang, *Mechanical Properties of Ti-6Al-4V Octahedral Porous Material Unit Formed by Selective Laser Melting*. Advances in Mechanical Engineering, 2012. **2012**.
34. Yang, L., *Experimental-assisted design development for an octahedral cellular structure using additive manufacturing*. Rapid Prototyping Journal, 2015. **21**(2): p. 168-176.
35. Hedayati, R., M. Sadighi, M. Mohammadi-Aghdam, and A.A. Zadpoor, *Effect of mass multiple counting on the elastic properties of open-cell regular porous biomaterials*. Materials & Design, 2016. **89**: p. 9–20.
36. Wauthle, R., B. Vrancken, B. Beynaerts, K. Jorissen, J. Schrooten, J.-P. Kruth, and J. Van Humbeeck, *Effects of build orientation and heat treatment on the microstructure and mechanical properties of selective laser melted Ti6Al4V lattice structures*. Additive Manufacturing, 2015. **5**: p. 77-84.
37. Park, S.-I., D.W. Rosen, S.-k. Choi, and C.E. Duty, *Effective mechanical properties of lattice material fabricated by material extrusion additive manufacturing*. Additive Manufacturing, 2014. **1**: p. 12-23.
38. Sekulovic, M. and R. Salatic, *Nonlinear analysis of frames with flexible connections*. Computers & Structures, 2001. **79**(11): p. 1097-1107.
39. Park, S.-i. and D.W. Rosen, *QUANTIFYING MECHANICAL PROPERTY DEGRADATION OF CELLULAR MATERIAL USING AS-FABRICATED VOXEL MODELING FOR THE MATERIAL EXTRUSION PROCESS*.
40. Rho, J.-Y., L. Kuhn-Spearing, and P. Zioupos, *Mechanical properties and the hierarchical structure of bone*. Medical engineering & physics, 1998. **20**(2): p. 92-102.
41. Zadpoor, A.A., J. Sinke, and R. Benedictus, *Elastoplastic deformation of dissimilar-alloy adhesively-bonded tailor-made blanks*. Materials & Design, 2010. **31**(10): p. 4611-4620.
42. Kidd, T., S. Zhuang, and G. Ravichandran, *In situ mechanical characterization during deformation of PVC polymeric foams using ultrasonics and digital image correlation*. Mechanics of Materials, 2012. **55**: p. 82-88.

43. Wang, Y. and A.M. Cuitiño, *Full-field measurements of heterogeneous deformation patterns on polymeric foams using digital image correlation*. International Journal of Solids and Structures, 2002. **39**(13): p. 3777-3796.
44. Hild, F. and S. Roux, *Digital image correlation: from displacement measurement to identification of elastic properties—a review*. Strain, 2006. **42**(2): p. 69-80.
45. Zadpoor, A.A., J. Sinke, and R. Benedictus, *Global and local mechanical properties and microstructure of friction stir welds with dissimilar materials and/or thicknesses*. Metallurgical and Materials Transactions A, 2010. **41**(13): p. 3365-3378.
46. Fleck, N., O. Olurin, C. Chen, and M. Ashby, *The effect of hole size upon the strength of metallic and polymeric foams*. Journal of the Mechanics and Physics of Solids, 2001. **49**(9): p. 2015-2030.
47. Olurin, O., N. Fleck, and M. Ashby, *Deformation and fracture of aluminium foams*. Materials Science and Engineering: A, 2000. **291**(1): p. 136-146.
48. Chen, C., N. Fleck, and T. Lu, *The mode I crack growth resistance of metallic foams*. Journal of the Mechanics and Physics of Solids, 2001. **49**(2): p. 231-259.
49. Amin Yavari, S., R. Wauthlé, A.J. Böttger, J. Schrooten, H. Weinans, and A.A. Zadpoor, *Crystal structure and nanotopographical features on the surface of heat-treated and anodized porous titanium biomaterials produced using selective laser melting*. Applied Surface Science, 2014. **290**: p. 287-294.

Figure Captions

Figure 1- Degrees of freedom of an octahedral unit cell

Figure 2- The volumes constructing a unit cell

Figure 3- Forces and moments required to cause (a) lateral displacement δ with no rotation at the free end of the beam, and (b) simple tension u

Figure 4- Loads applied to strut AB to cause deformation mode $q_1 = 1$ and $q_2 = 0$ for Euler-Bernoulli beam theory

Figure 5- Loads applied to struts (a) AB and (b) BB' to cause deformation mode $q_1 = 0$ and $q_2 = 1$ for Euler-Bernoulli beam theory

Figure 6- The octahedral lattice structure: (a) front view, (b) oblique view

Figure 7- Additively manufactured cylindrical specimens made (a) horizontally, (b) vertically, and (c) 45° angled for obtaining the bulk material properties of Khaki filament

Figure 8- Additively manufactured octahedral lattice structures with (a) $r/l=0.25$, (b) $r/l=0.2$, (c) $r/l=0.15$, and (d) $r/l=0.1$

Figure 9- Additively manufactured octahedral single unit cells with (a) $r/l=0.05$, (b) $r/l=0.1$, (c) $r/l=0.2$, and (d) $r/l=0.25$

Figure 10- Load-displacement curves for (a) single unit cell and (b) lattice structure specimens with different radius to strut length ratios

Figure 11- Comparison of analytical, numerical, and experimental vs. relative density for (a) elastic modulus, (b) Poisson's ratio, and (c) yield stress

Table 1- Elastic properties of cylindrical specimens made of Khaki filaments

	Vertically-made	Horizontally-made	45°-made
Elastic modulus (GPa)	2.04 ± 0.09	2.49± 0.01	2.42 ± 0.10
Yield stress (MPa)	68.82 ± 0.44	56.16 ± 0.49	65.00 ± 0.14

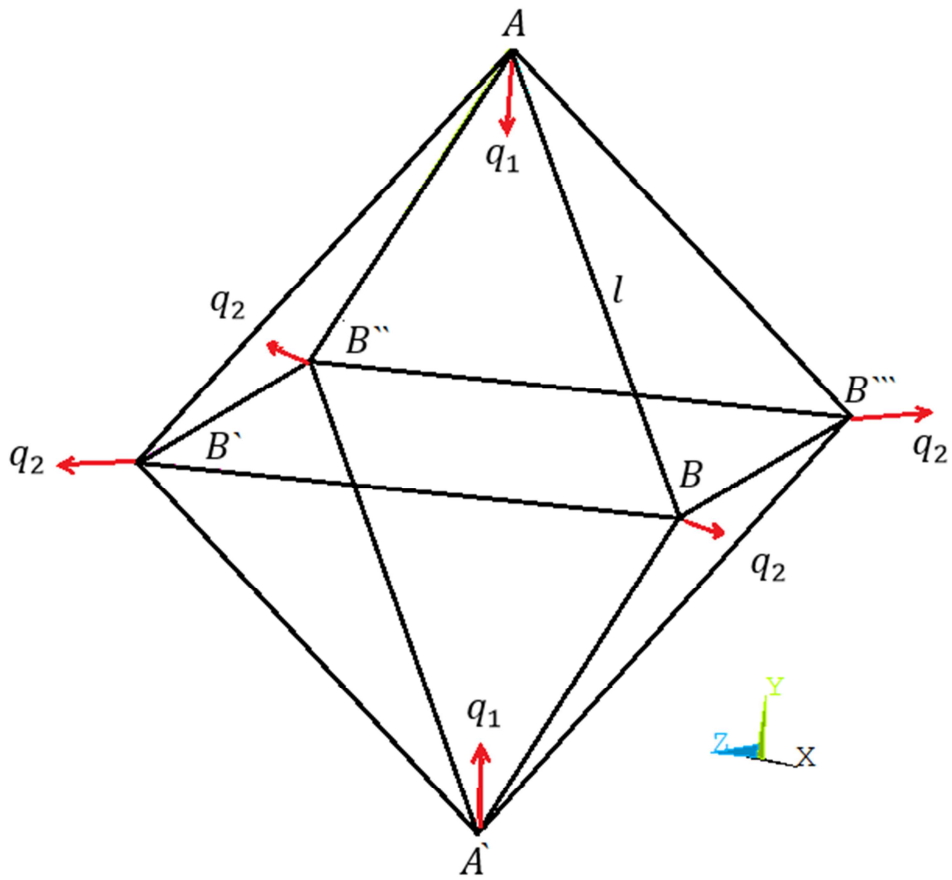
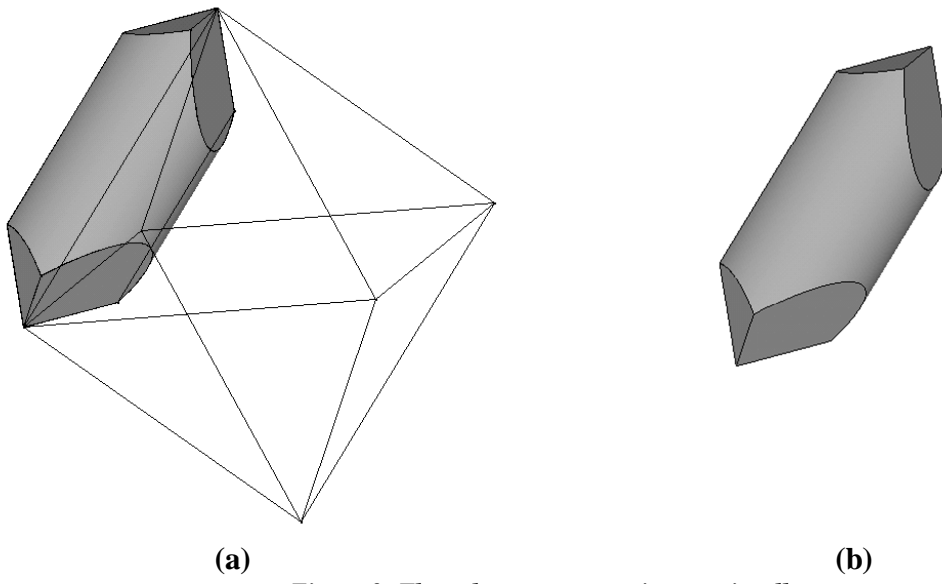


Figure 1- Degrees of freedom of an octahedral unit cell



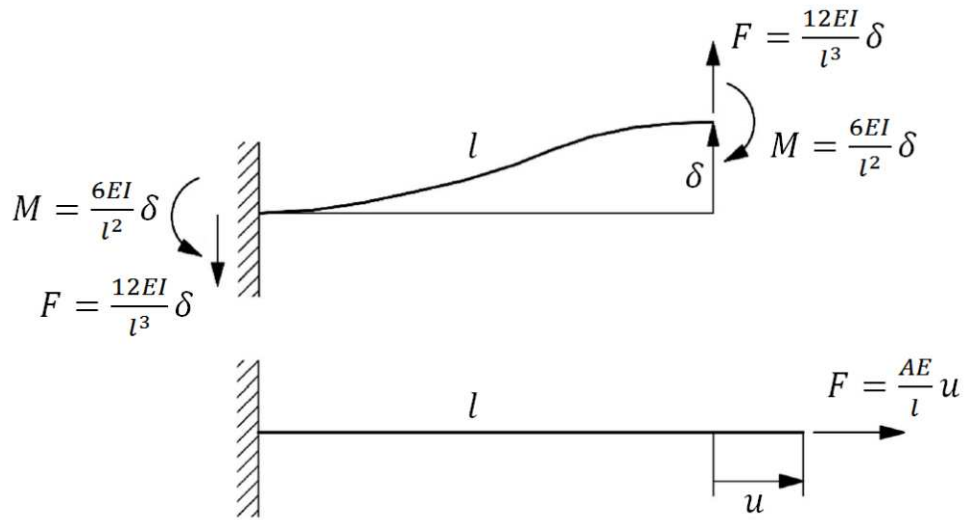


Figure 3- Forces and moments required to cause (a) lateral displacement δ with no rotation at the free end of the beam, and (b) simple tension u

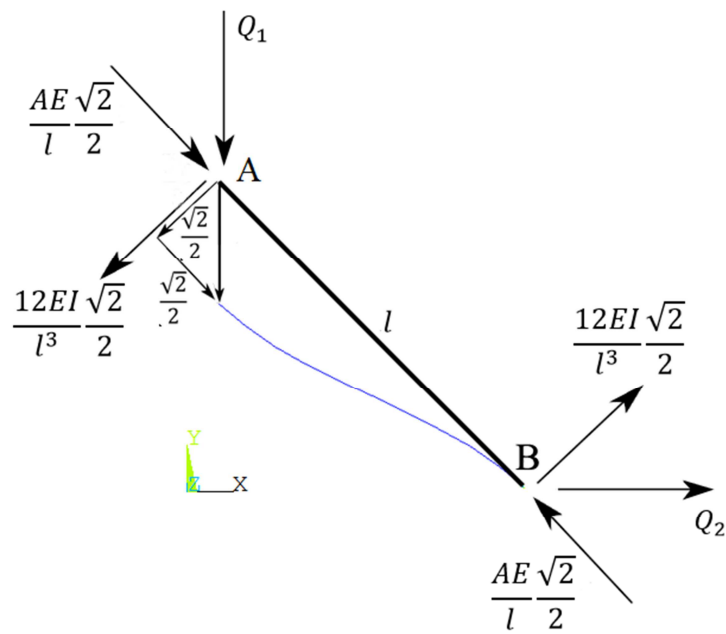


Figure 4- Loads applied to strut AB to cause deformation mode $q_1 = 1$ and $q_2 = 0$ for Euler-Bernoulli beam theory

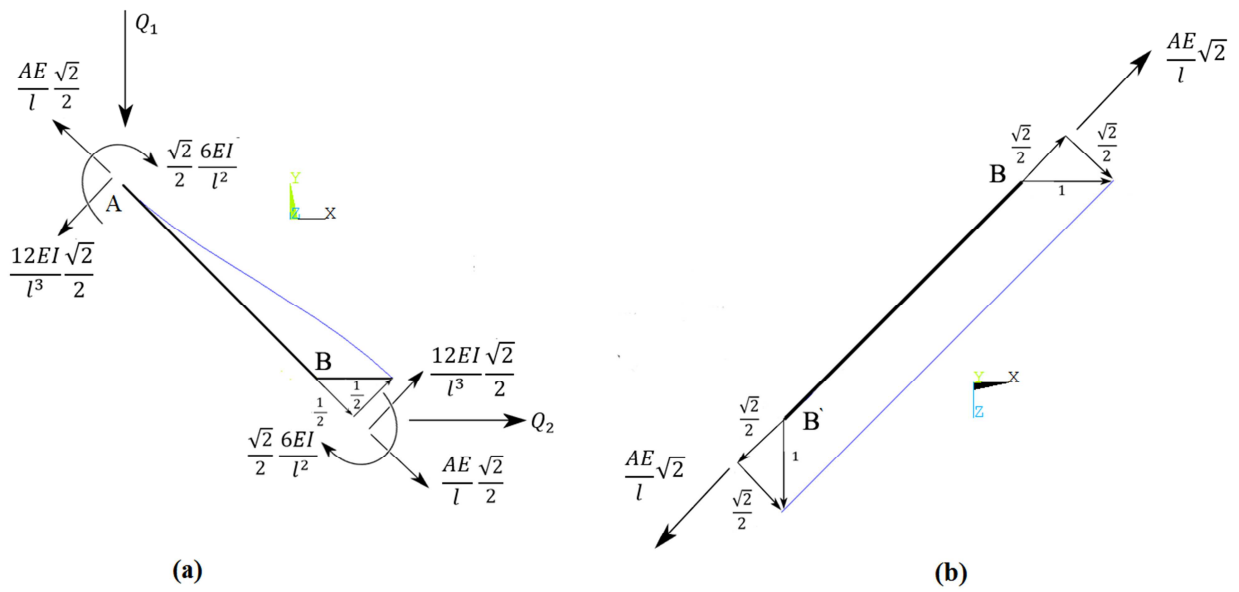
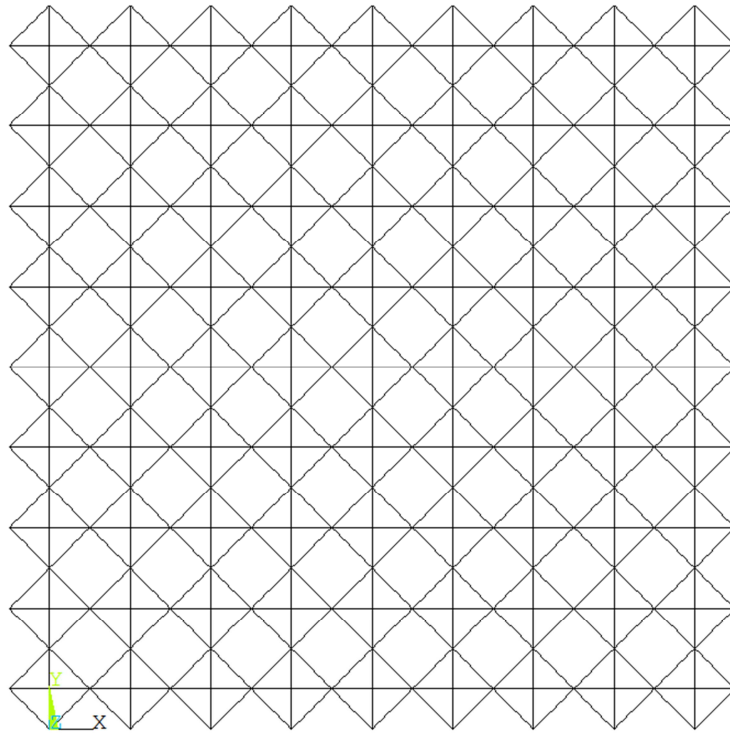
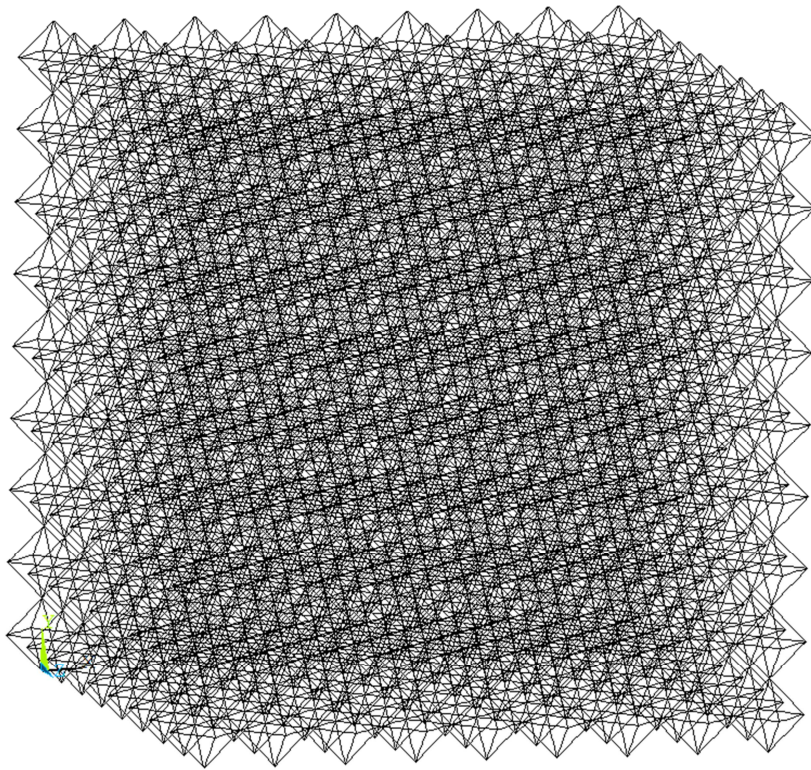


Figure 5- Loads applied to struts (a) AB and (b) BB' to cause deformation mode $q_1 = 0$ and $q_2 = 1$ for Euler-Bernoulli beam theory



(a)



(b)

Figure 6- The octahedral lattice structure: (a) front view, (b) oblique view

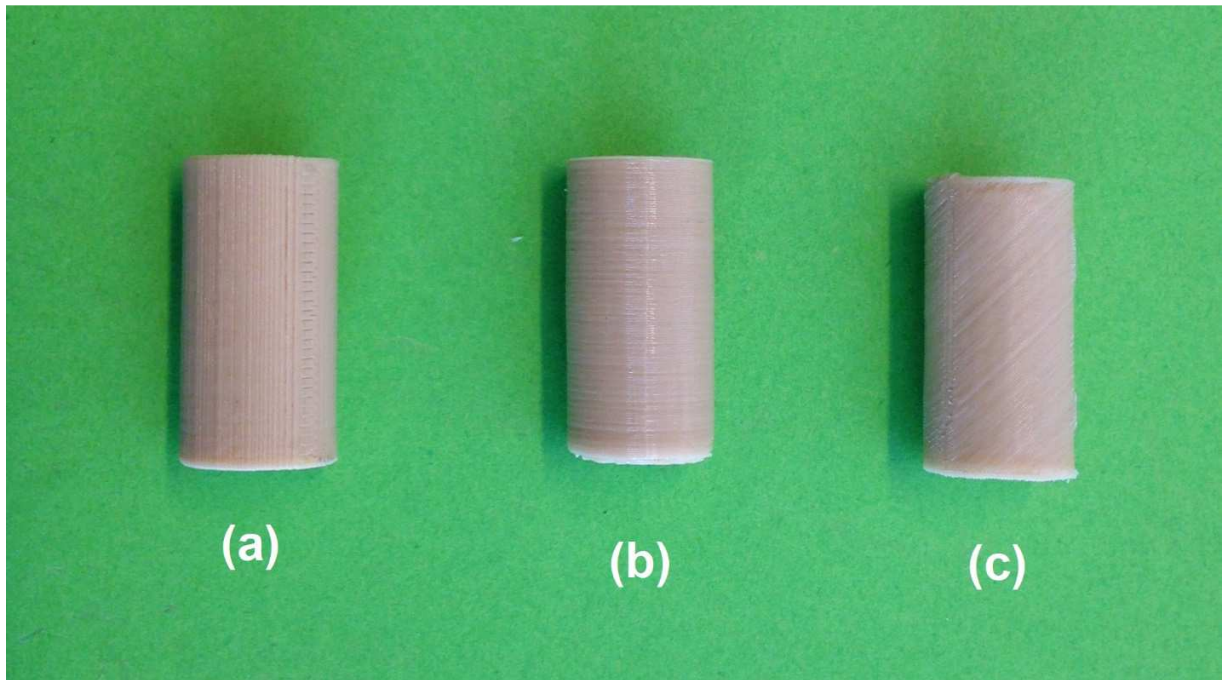


Figure 7- Additively manufactured cylindrical specimens made (a) horizontally, (b) vertically, and (c) 45° angled for obtaining the bulk material properties of Khaki filament

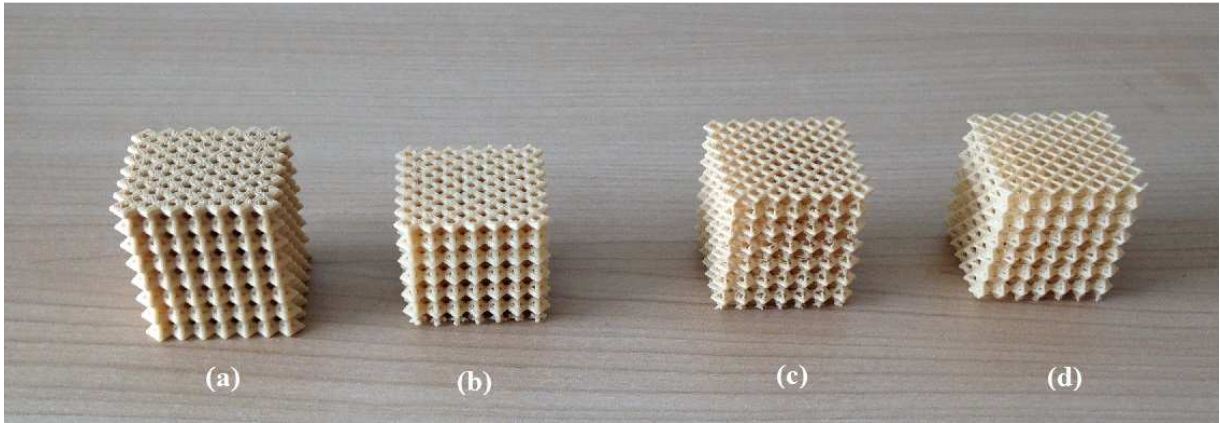


Figure 8- Additively manufactured octahedral lattice structures with (a) $r/l=0.25$, (b) $r/l=0.2$, (c) $r/l=0.15$, and (d) $r/l=0.1$

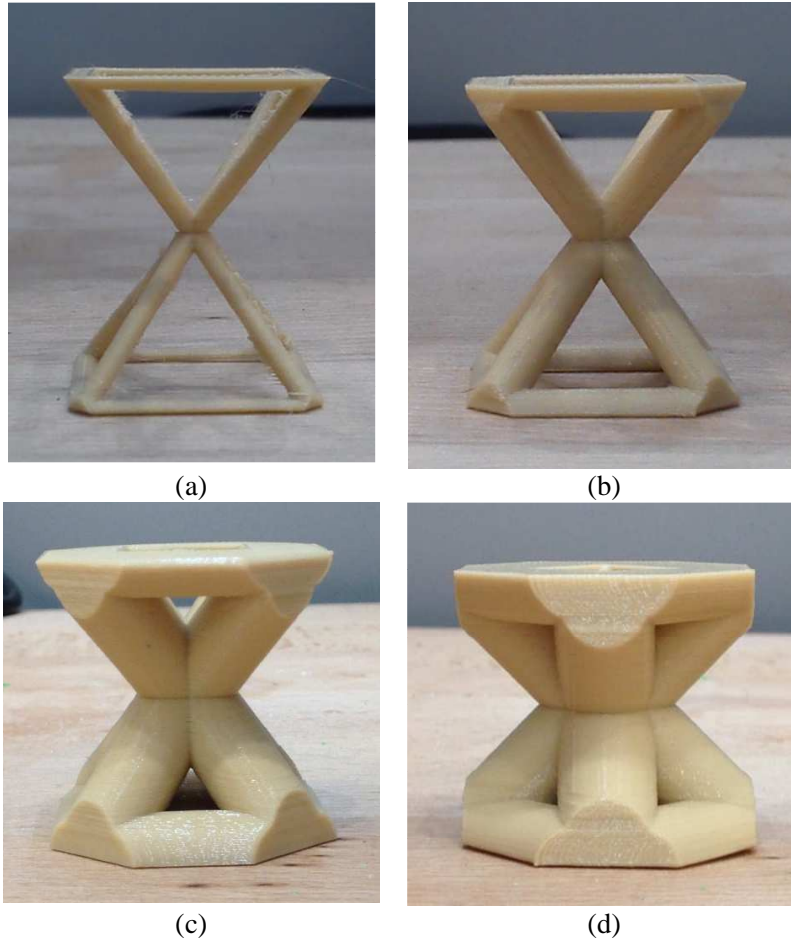
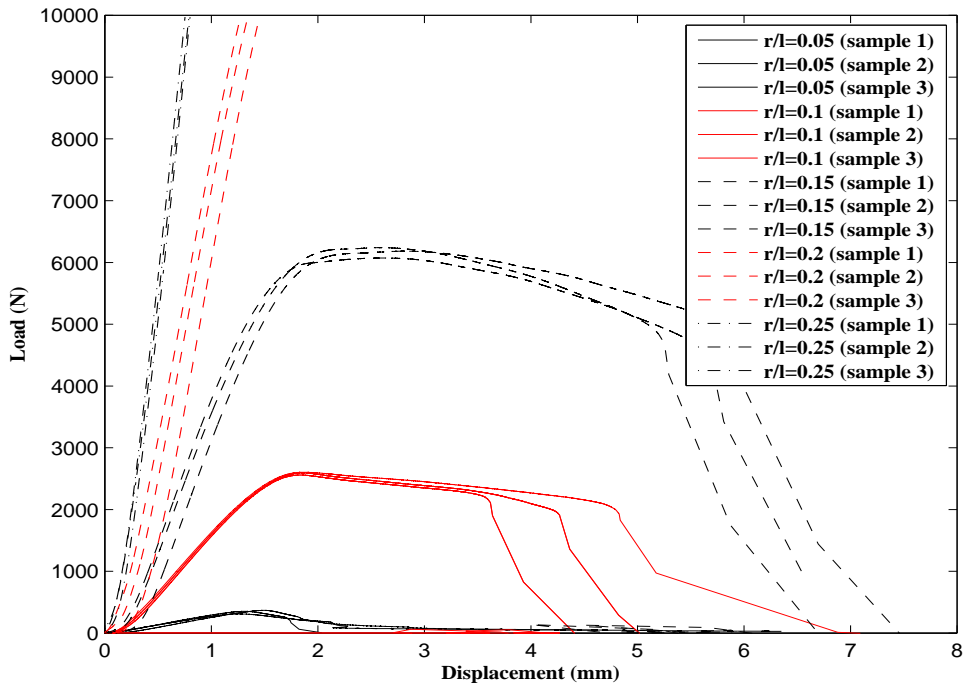
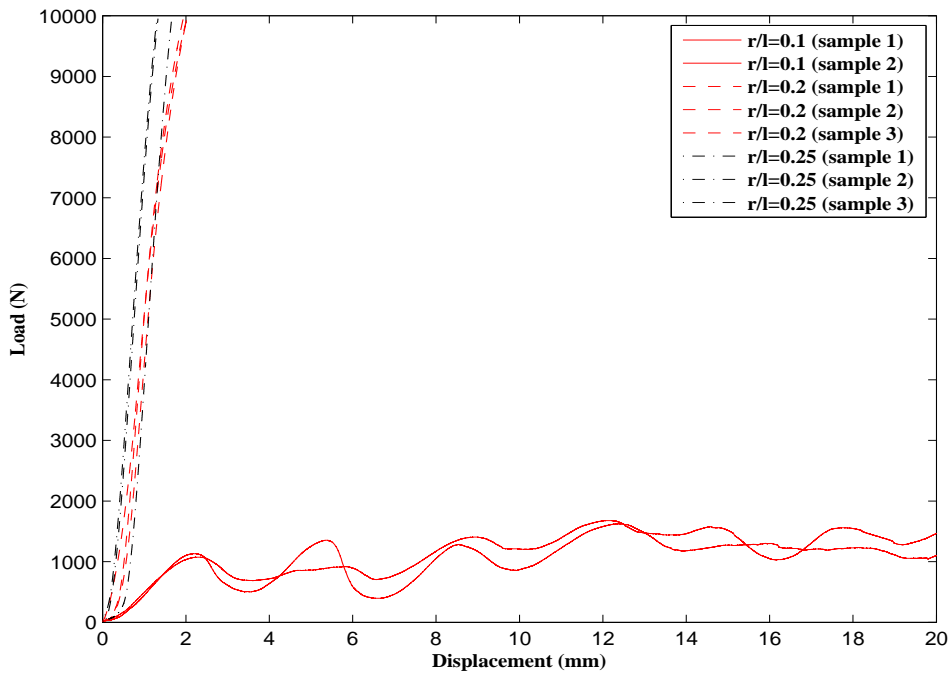


Figure 9- Additively manufactured octahedral single unit cells with (a) $r/l=0.05$, (b) $r/l=0.1$, (c) $r/l=0.2$, and (d) $r/l=0.25$

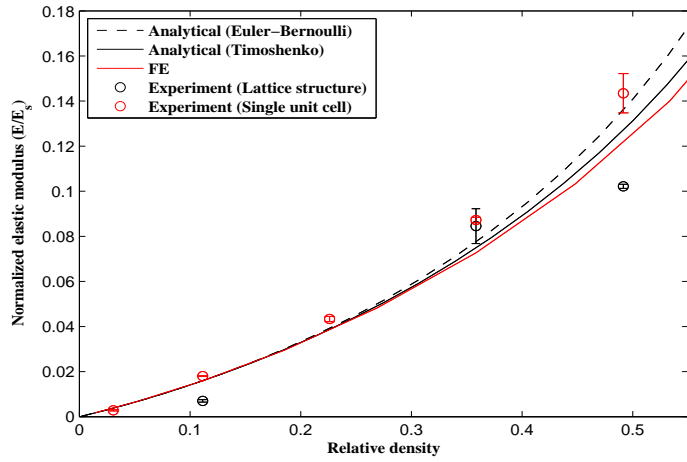


(a)

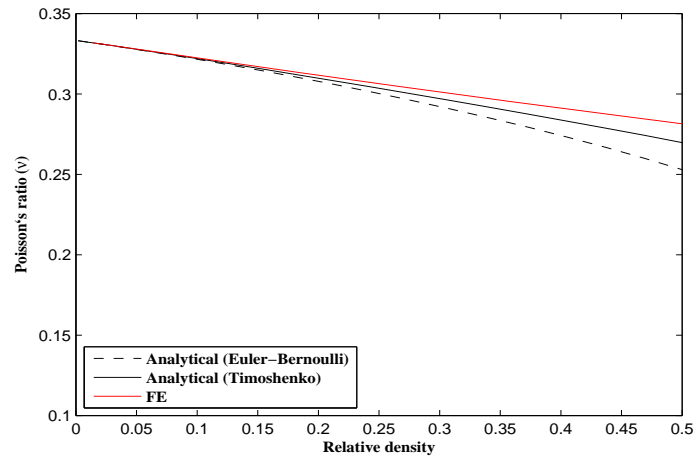


(b)

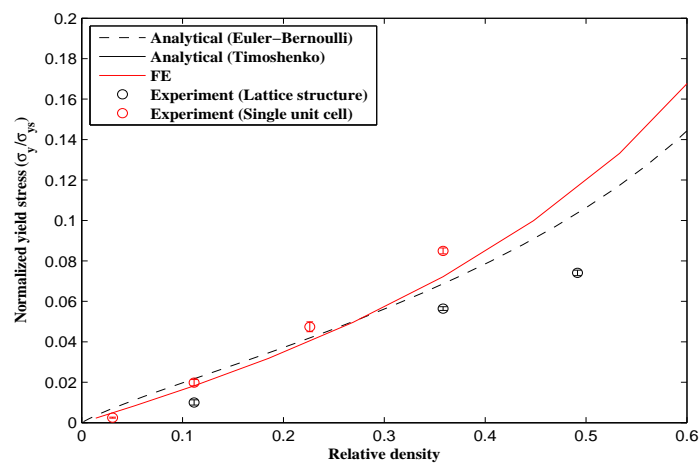
Figure 10- Load-displacement curves for (a) single unit cell and (b) lattice structure specimens with different radius to strut length ratios



(a)



(b)



(c)

Figure 11- Comparison of analytical, numerical, and experimental vs. relative density for (a) elastic modulus, (b) Poisson's ratio, and (c) yield stress